WILEY-VCH

DOI: 10.1002/ ((please add manuscript number))
Article type: Full paper

Energy-Sensitive GaSb/AlAsSb Separate Absorption and Multiplication Avalanche Photodiodes for X-Ray and Gamma-Ray Detection

Bor-Chau Juang, Andrew Chen, Dingkun Ren, Baolai Liang, David L. Prout, Arion F. Chatziioannou, and Diana L. Huffaker

Dr. B. C. Juang, A. Chen, Dr. Dingkun Ren, Prof. D. L. Huffaker
Department of Electrical and Computer Engineering
University of California – Los Angeles
Los Angeles, California 90095, USA

Dr. B. L. Liang
California NanoSystems Institute
University of California – Los Angeles
Los Angeles, California 90095, USA
E-mail: bliang@cnsi.ucla.edu

Dr. D. L. Prout, Prof. A. F. Chatziioannou
Department of Molecular and Medical Pharmacology
Crump Institute for Molecular Imaging
University of California – Los Angeles
Los Angeles, California 90095, USA

Keywords: Semiconductor heterostructures; SAM-APDs; X-rays detection; Gamma-rays

We demonstrate antimony-based (Sb-based) separate absorption and multiplication avalanche photodiodes (SAM-APDs) for X-ray and gamma-ray detection, which are composed of GaSb absorbers and large bandgap AlAsSb multiplication regions in order to enhance the probability of stopping high-energy photons while drastically suppressing the minority carrier diffusion. Well-defined X-ray and gamma-ray photopeaks are observed under exposure to ^{241}Am radioactive sources, demonstrating the desirable energy-sensitive detector performance.

Spectroscopic characterizations show a significant improvement of measured energy resolution due to reduced high-peak electric field in the absorbers and suppressed nonradiative recombination on surfaces. Additionally, the GaSb/AlAsSb SAM-APDs clearly exhibit energy response linearity up to 59.5 keV with a minimum full-width half-maximum of 1.283 keV. A further analysis of the spectroscopic measurement suggests that the device performance is intrinsically limited by the noise from the readout electronics rather than that from the photodiodes. This study provides a first understanding of Sb-based energy-sensitive SAM-APDs and paves the way to achieving efficient detection of high-energy photons for X-ray and gamma-ray spectroscopy.

1. Introduction

Various photodetection systems for high-energy photons have been developed in recent years with wide commercial and scientific applications [1-10]. Among them, separate absorption and multiplication avalanche photodiodes (SAM-APDs) composed of photoabsorbers and large bandgap multiplication regions are advantageous for achieving high-efficient and low-noise photodetection with high resolution [11-13]. Such a detector architecture can be also applied to energy-sensitive gamma-ray and X-ray detection. A GaAs/AlGaAs SAM-APD comprised of a 4.5 μm absorption region and a staircase-like multiplication region has been developed for X-ray photodetection [14]. Meanwhile, a similar GaAs/$Al_{0.8}Ga_{0.2}As$ SAM-APD structure has been also demonstrated to detect soft X-rays at 5.9 keV with a full-width half-maximum (FWHM) of 1.08 keV [15]. However, its spectroscopic characterizations show an undesired secondary peak located at the energy lower than the 5.9 keV peak. This is because of (1) different degrees of impact ionization experienced by the electrons and holes [16-18]; (2) insufficient layer thickness ratio [19]; and (3) inadequate difference of pair creation energy (PCE) between GaAs and AlGaAs [20,21]. Indeed, the absorption efficiency can be improved by simply increasing the thickness of the

absorption layer. Unfortunately, the commonly used (Al)GaAs semiconductors are not able to concurrently offer high-*Z* (i.e., high atomic number) absorption and large PCE difference within SAM structures for high energy X-ray or gamma-ray detection.

Alternatively, the antimony-based (Sb-based) SAM-APD structure with high-*Z* GaSb and large bandgap AlAsSb is promising. GaSb absorbers can provide a much higher probability than GaAs to stop X-ray and gamma-ray photons at a given energy due to a relatively higher *Z* [22]. In addition, the GaSb/AlAsSb material system provides a larger dissimilarity in both PCE and absorption efficiency [23,24]. This allows for a significant suppression of spurious photopeaks, which are generated outside the intended absorption regions. The combination of these unique capabilities shows promise for achieving X-ray and gamma-ray detectors with high spectroscopic performance. To prove the concept, we develop GaSb/AlAsSb SAM-APDs composed of 2 μm GaSb absorbers and AlAsSb digital alloy multiplication regions to detect X-ray and gamma-ray photopeaks under iradiation from ^{241}Am sources. Due to the reduced high-peak electric field in the absorbers and suppressed nonradiative recombination on surfaces, detection linearity up to 59.5 keV is clearly observed with the minimum FWHM of 1.283 keV at 59.5 keV. Finally, we perform a detalied analysis of noise factors to understand the intrinsic limit of high-energy photodetection.

2. Results and Discussion

2.1. Device design

The schematic diagram of a GaSb/AlAsSb SAM-APD is illustrated in Figure 1. An $AlAs_{0.08}Sb_{0.92}$ digital-alloy (hereinafter AlAsSb) PIN junction with a *p*-AlAsSb field-control (FC) layer was firstly formed, followed by growth of a 2 μm GaSb absorber. A 50 nm $Al_{0.4}Ga_{0.6}Sb$ (hereafter AlGaSb) layer was then introduced as surface barrier to eliminate the carrier loss [25]. The same absorber thickness was used to match that of a previously reported GaSb PIN diode for

a fair comparison of their spectroscopic performance evaluation [1]. In this GaSb/AlAsSb heterostructure, the majority of the electric field can be tightly confined within the large bandgap AlAsSb multiplication region, while the magnitude of electric field is sufficiently low in the high-*Z* GaSb absorber. The low field strength can minimize the field-assisted current components resulting from field-enhanced Shockley–Read–Hall (SRH) nonradiative recombination and band-to-band tunneling (BTBT) [26]. It can also eliminate the premature impact ionization process in the absorber. To obtain the desired electric field profile, we optimized the thickness of the *p*-AlAsSb FC layer to 125 nm and its nominal charge density to 1.25×10^{12} cm^{-2}.

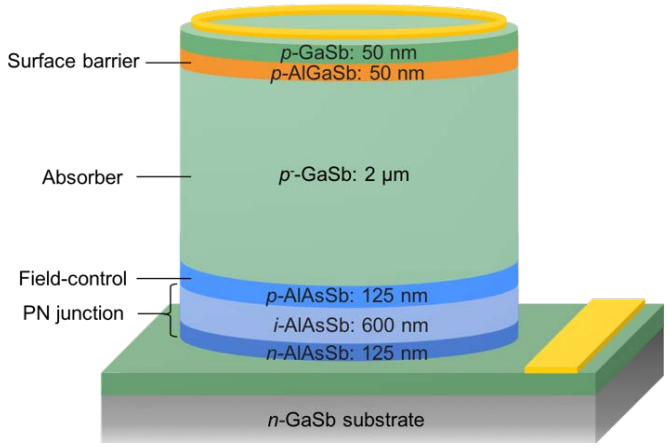

Figure 1 Schematic diagram of the GaSb/AlAsSb SAM-APD structure with a 2 μm GaSb absorber.

2.2. Material fabrication and characterizations

The GaSb/AlAsSb SAM-APD structure shown in Figure 1 was grown on a *n*-type GaSb (001) substrate by a Veeco Gen930 solid-source molecular-beam epitaxy (MBE) reactor. The AlAsSb films were realized via digital alloy growth technology by periodically alternating the arsenic (As) and antimony (Sb) shutters while maintaining a steady aluminum (Al) flux, resulting in an equivalent AlSb/AlAs sequence of 4.0/0.44 monolayers [27]. Figure 2(a) shows a high-resolution cross-sectional transmission electron microscopy (TEM) image of the AlAsSb digital alloy layer and its diffraction pattern. We observe uniformly distributed AlAsSb alloy layers

without any sign of AlAs/AlSb layer separation. This suggests that the alternating shutter sequence does not produce modulated contrast. The lattice spacing of the *p*-AlAsSb layer was measured as 0.61 nm, which indicates a perfect lattice matching to the GaSb absorber. In addition, the diffraction pattern of the *p*-AlAsSb layer also affirms its crystalline structure, as shown in Figure 2(a). Furthermore, we performed photoluminescence (PL) characterization of AlAsSb digital alloys at 7K, as shown in Figure 2(b). We observed an anomalous emission around 1.29 eV as well as a strong narrow peak at 1.59 eV along with a weak side band peaking around 1.86 eV. Since AlAsSb is an indirect bandgap material and its minimum bandgap is within the *X* valley (E^X), we assign the strong emission at 1.59 eV as the carrier recombination from the *X*-band. The side band peaking at 1.84 eV is likely due to the transition from the *Γ*-band. Additionally, our AlAsSb digital alloy has a similar bandgap compared with the reported value given in a previous study [28].

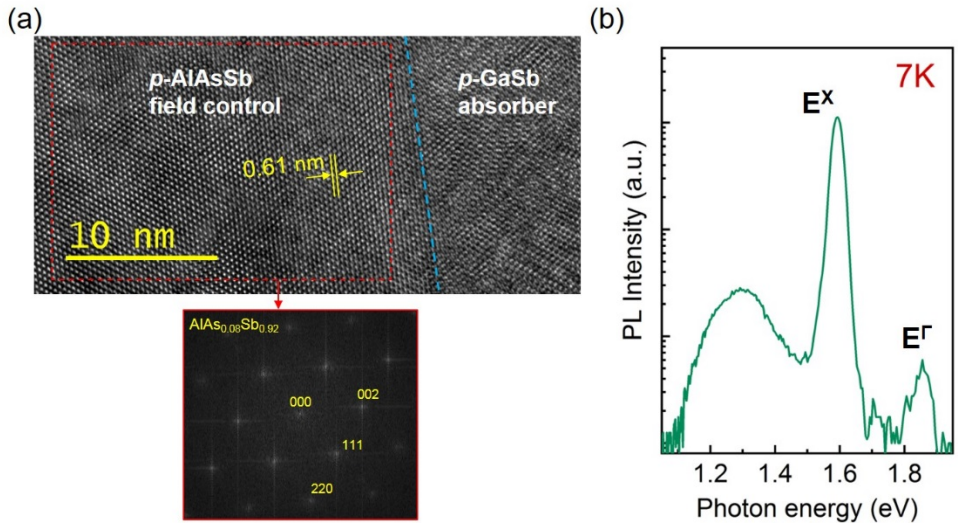

Figure 2 (a) High-resolution cross-sectional TEM of the GaSb/AlAsSb interface and corresponding diffraction pattern of the AlAsSb digital-alloy multiplication layer. (b) Low-temperature (7 K) PL emission from AlAsSb digital alloys.

2.3. Electrical characterization

The device characterizations were performed at liquid-nitrogen cooled temperature, i.e., 77 K, to minimize the noise from dark carriers. Capacitance-voltage (C-V) measurements were firstly carried out to extract the width of the depletion region and estimate the distribution of electric field as a function of reverse bias, as shown in Figure 3. The C-V curve in low bias regime is relatively flat, which indicates that the *i*-AlAsSb layer (background doping ~6×10^{14} cm^{-3} based on the $1/C^2$-V analysis) is fully depleted at zero bias while the depletion region extends into the FC layer. The electric field is fully confined within the AlAsSb multiplication region. With increasing reverse bias to approximately 7.5 V, the device capacitance shows a rapid drop, meaning that the edge of the depletion region, or the electric field, has extended into the GaSb absorber.

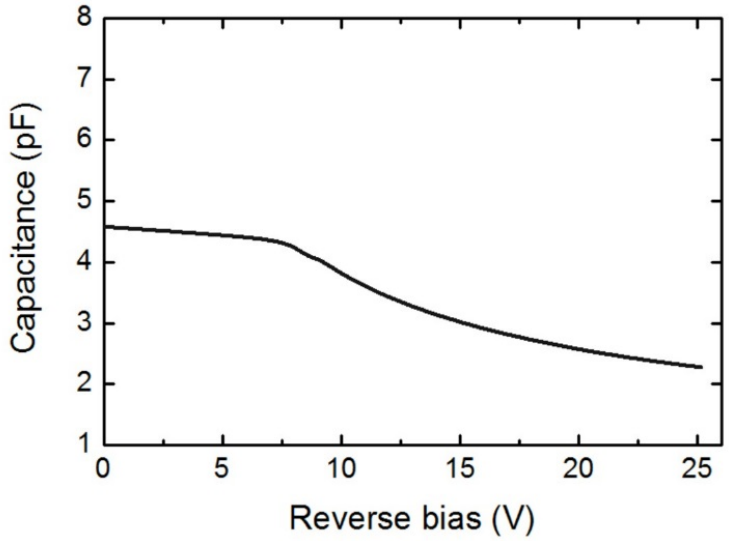

Figure 3 Capacitance characteristics of the GaSb/AlAsSb SAM-APD at 77 K. The edge of depletion region reaches GaSb absorber at 7.5V. The mesa size is 200 μm.

Next, photocurrent-voltage characterizations were carried out by a continuous-wave (CW) laser at 1310 nm, which allowed electron-hole pairs to be generated only in the GaSb absorbers. Clearly, the characteristics of photocurrent are different from those of InGaAs/InP [29,30] or InGaAs/InAlAs SAM-APDs [31-34]. As shown in Figure 4(a), we observe a two-stage increase in

photocurrent. In the low bias regime, photoresponse is limited by the inactive GaSb region. With increasing reverse bias up to 7.5 V, the photocurrent shows an abrupt increase, which corresponds to the reach through voltage shown in the C-V characteristics (Figure 3). Interestingly, with further increasing reverse bias beyond 7.5 V, we observe a second increase in photocurrent of a few orders of magnitude, followed by an apparent photocurrent plateau. Such plateau regime can be attributed to the full carrier collection at unity gain. The device responsivity was measured as 0.625 A/W using the primary photocurrent within this regime. This value is higher than 0.578 A/W given by the GaSb PIN devices [1]. The improvement in responsivity can be attributed to the suppressed surface recombination due to additional AlGaSb window layers. Furthermore, a typical behavior of carrier multiplication is observed near the avalanche breakdown at 28 V.

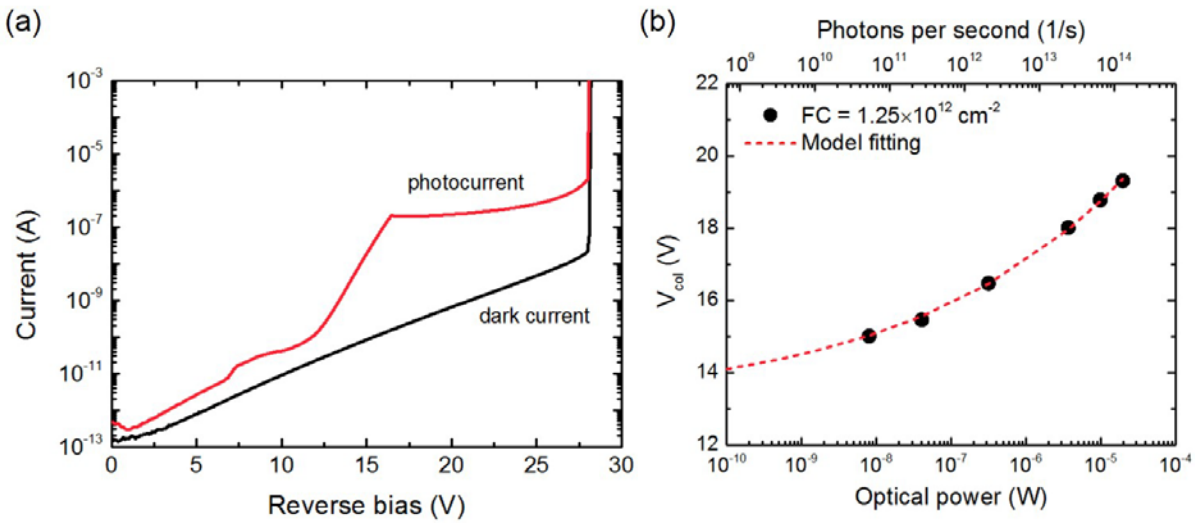

Figure 4 (a) Dark current characteristics of the 200 µm GaSb/AlAsSb SAM-APD at 77 K. (b) Extracted V_{col} as a function of incident optical power and number of photons per second.

The two-stage increase in photocurrent can be explained as follows. At a reverse bias near 7.5 V, the electric field begins to build up in the GaSb absorber, and only the carriers with sufficient kinetic energy are able to travel across the GaSb-AlAsSb interface barrier. As a result, the first increase in photocurrent results from the onset of collection for carriers generated in the

absorber. Once a certain electric field strength is established in GaSb, i.e., at reverse bias of 16 V, all photo-generated carriers can travel across the heterointerface and contribute to the photocurrent. In addition, we notice that the voltage (V_{col}) that allows a full collection of photo-generated carriers is strongly dependent on the incident optical power (i.e., number of photo-generated carriers in the absorber), as shown in Figure 4(b). We surmise that the two-stage increase in photocurrent is related to carrier transport dynamics such as electron-to-electron scattering due to increased number of carriers. The increasing V_{col} with increasing photogenerated carriers can be well described by an empirical model $V_{col} = V_{col}^{0} + aN_{ph}^{b}$, where N_{ph} is the number of photons available to create electron-hole pairs, and a and b are fitting parameters. The peak density of electron-hole pairs created in a burst by a single X-ray or gamma-ray (on average, $10^{3\text{-}4}$ of electron-hole pairs per photon) is similar to that by a 1310 nm CW laser with the power of tens of nW, therefore we expect that V_{col} is approximately close to 15 V.

The temporal response of the GaSb/AlAsSb devices (mesa size of 200 μm) was carried out using a pulsed laser at 1310 nm (pulse width of 20 ps and average power of 4.3 μW) and a 20 GHz oscilloscope (50 GS/s). The signal rise time (10% to 90% of the pulse amplitude) is approximately 100-110 ps with little variation at different reverse bias beyond V_{col}. The nearly constant rise time characteristic suggests that the temporal response of the device is not limited by the carrier diffusion process and the GaSb absorption region is partially depleted at the avalanche breakdown.

Additionally, we note that the dark current increases monotonically with increasing reverse bias and exhibits an abrupt breakdown at 28 V. Since there is no sign of apparent increase in dark current beyond 7.5 V, the dark current does not result from either the generation-recombination process in the GaSb absorber or the BTBT process. A negligible surface leakage current is found

near the breakdown by correlating the total current with the perimeter-to-area ratio (not shown). It is possible to further suppress the attainable dark current floor by improving surface passivation.

2.4. Radiation characterization

The GaSb/AlAsSb SAM-APDs were wire-bonded and tested with a 0.74 MBq ^{241}Am radioactive source at 77 K. The spectra at different reverse bias voltages are shown in Figure 5, where the pulser signals are used as references. We observe different stages of carrier collection with a progression of photopeaks in multi-channel analyzer (MCA) channels by increasing reverse bias. Below 7.5V, the spectra remain unchanged with photopeaks registered at similar MCA channels, suggesting that the collected carriers are mainly from the AlAsSb layer since the electric field has not built up in the GaSb absorber. At an increased reverse bias, photopeak signals at higher channel numbers start to take place with increasing frequency. Since GaSb has a relatively small PCE, a larger pulse height is generated compared with those from the AlAsSb layer. Once the reverse bias reaches 14 V (beyond the actual V_{col}), the carriers can be efficiently collected, leading to well-defined photopeaks in all signature lines, i.e., 13.9 keV (GaSb), 17.8 keV (GaSb), and 20.8 keV (GaSb), shown in the energy spectra.

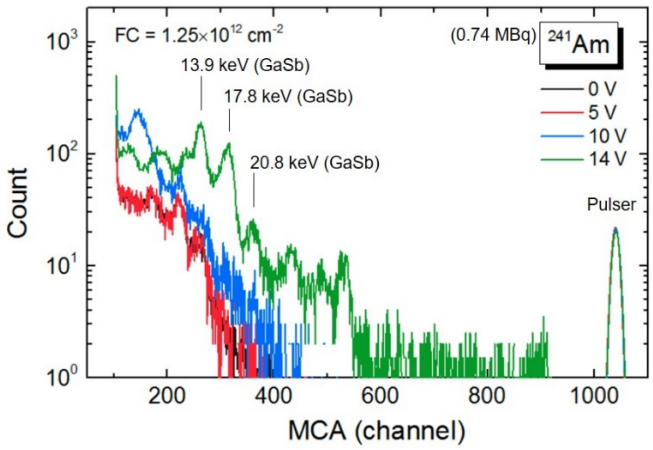

Figure 5 ^{241}Am spectra acquired by the GaSb/AlAsSb SAM-APDs under different reverse bias. The pulser peaks (overlapped by each other) serve as references to exhibit the progression of photopeaks.

We acquired the second spectrum using another ^{241}Am source with a stronger activiy (1.55 GBq) at 77 K, as shown in Figure 6(a), to obtain better statistics at gamma-ray energy [1]. The GaSb/AlAsSb SAM-APD at reverse bias of 14 V shows a distinct peak at 59.5 keV with a FWHM of 1.283±0.082 keV, which is much narrower than the 1.789±0.057 keV of GaSb PIN photodiodes (Figure 6(b)) in our previous report [1]. In addition, we observe more signature energy lines, which are well-defined and similar to the ones detected by the GaSb PIN photodiodes [1]. Those energy lines include (1) Ga Kα escape peak at 50.3 keV; (2) Sb Kα escape peak at 33.2 keV; (3) Sb Kβ escape peak at 29.8 keV; (4) Sb Kα characteristic X-ray peak at 26.3 keV; (5) Ga Kα escape peak at 17.1 keV; and (6) Ga Kα characteristic X-ray peak at 9.3 keV. Notably, the photopeaks generated from the AlAsSb multiplication region are not shown in the spectrum (Figure 6(a)). This is likely because the signals from the AlAsSb region are less significant than those generated from the GaSb absorber. This further indicates that the large differences in PCE and absorption efficiency between GaSb and AlAsSb have successfully eliminated spurious photopeaks in the intended spectrum regime and facilitated the identification of energy lines.

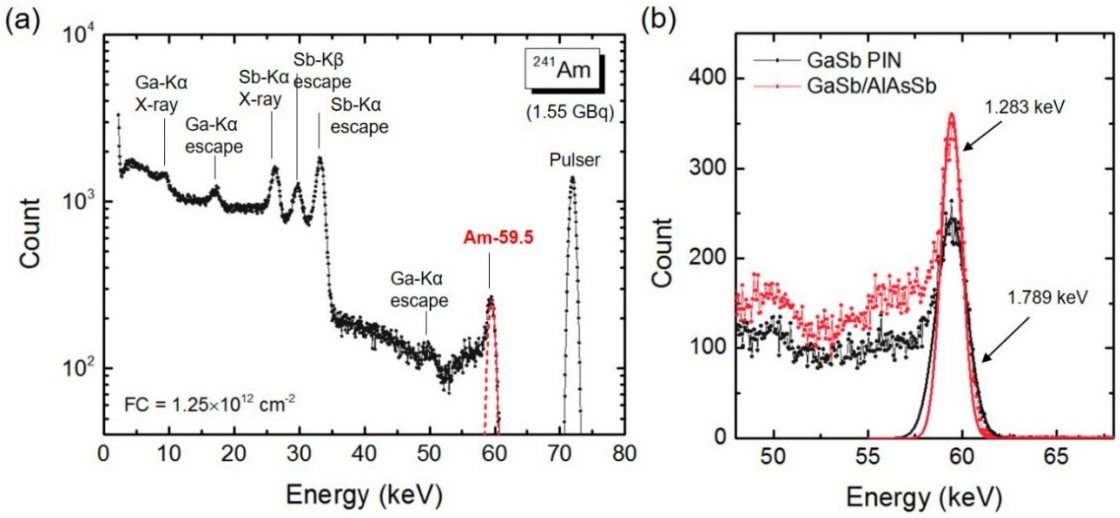

Figure 6 (a) 77 K 1.55 GBq ^{241}Am spectrum detected by the GaSb/AlAsSb SAM-APDs at reverse bias of 14 V. (b) FWHM comparison of 59.5 keV photopeaks obtained by the GaSb/AlAsSb SAM-APDs and the GaSb PIN photodiodes (reference devices) with the same photon counts.

2.5. Noise analysis

As shown in Figure 7(a), the energy resolution at 59.5 keV continues to improve when the reverse bias approaches V_{col}, where the best FWHM is 1.283±0.082 keV. However, with further increasing bias, the FWHM becomes larger. To understand the underlying mechanism, we studied the noise performance by decoupling three noise components–Fano noise, electronic noise and excess noise–as a function of reverse bias (Figure 7(b)). The electronic noise remains relatively the same across the entire bias range, indicating that it is dominated by the leakage current and the stray capacitance from the readout system rather than the detectors. Furthermore, the system-dominated electronic noise with FWHM of 1.125±0.003 keV (163 electron rms) was measured at 14 V. If this value can be further reduced to 20 electron rms [35,36] by optimizing the entire system, we can expect an overall FWHM of 627 eV at 59.5 keV.

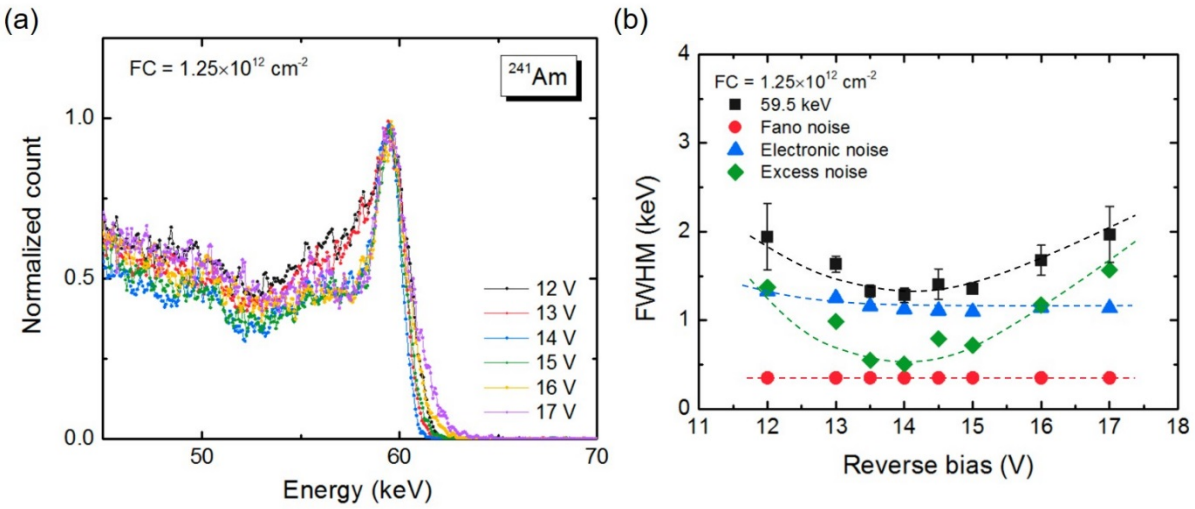

Figure 7 (a) The 59.5 keV peak at different bias. (b) Variation of the three noise components of the 59.5 keV peak as a function of reverse bias.

Additionally, the decoupled excess noise approaches a minimum at about 13 – 15 V, where the full carrier collection occurs. In the low bias regime, the relatively high excess noise is likely due to the noise from incomplete collection of the carriers. In other words, the carriers with insufficient kinectic energy cannot travel across the GaSb/AlAsSb heterointerface barrier. With increasing bias, the excess noise increases again when the device is biased beyond 15V. Since we do not observe similar trends from other photopeaks, the increase is not likely due to impact ionization within the GaSb or AlAsSb region. The origin of this behavior is still unclear and needs to be further investigated.

Compared with convential PIN photodiodes, our AlAsSb/GaSb SAM-APDs show improved energy-resolving capability due to a significant reduction of excess noise in the GaSb absorbers. At the 59.5 keV peak, the excess noise is 508 eV at 14V, which is well-improved from the 1245 eV of the GaSb PIN photodiodes at 2 V [1]. This property can be better interpreted by the electric field distribution in the GaSb absorber. Due to the heterostructure device structure, the electric field can be properly controlled, which limits any field-assisted process and thus suppresses

the excess noise. Even though the surface leakage current is the limiting factor of signal-to-noise ratio (SNR), it can be still improved by tailoring the electric field distribution. In addition, the excess noise exhibits no photon energy dependence, as shown in Figure 8, which supports that the excess noise is not dominated by incomplete carrier collection. Lastly, the AlGaSb window layer can also effectively lead to less surface leakage via nonradiative recombination.

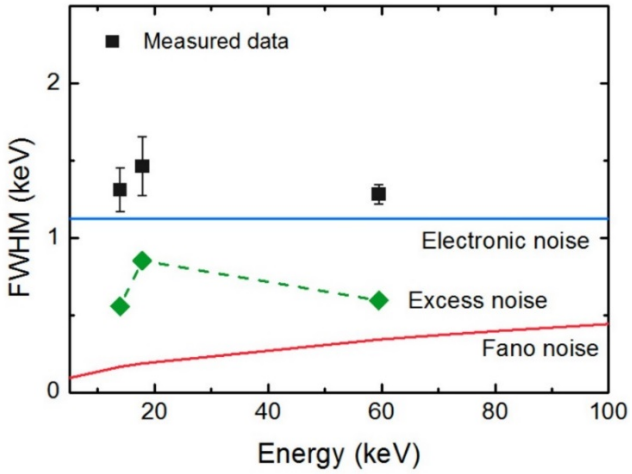

Figure 8 The measured FWHM of the three signature photopeaks obtained by the AlAsSb/GaSb device under 14 V and the respective decoupled noise components.

2.6. Toward high-performance energy-sensitive SAM-APDs

The purpose of this work is to show that the GaSb/AlAsSb SAM-APD platform with high-*Z* GaSb absorbers and large bandgap AlAsSb has the potential to provide performance **improvements for energy-sensitive photodetection. Table 1 shows a cross-comparison of device architectures and** energy resolutions at 59.5 keV among GaSb-based and other high-Z **detectors. In this work, we developed a SAM-APD device platform with the high-**Z **GaSb absorber, which structure can be** readily **grown** using **the standard MBE technique. In contrast, TlBr and CdTe detectors suffer from hole tailing and significant nonradiative recombination due to defects resulting from low-quality crystal growth. In terms of 59.5 keV**

energy resolution, the GaSb/AlAsSb devices offer a minimum FWHM value of 1.283 keV at a reduced temperature of 77K**,** which is **slightly higher than the best value of 0.95 keV given by GaAs PIN diodes** without cooling**. The next challenge** to the **GaSb/AlAsSb devices is** how **to** suppress **noise to** achieve an improved **energy resolution and** a higher **operating temperature. One solution is to** improve the surface passivation by **introducing the sulfur treatment along with the suitable large-bandgap dielectric layers to protect the exposed GaSb mesa sidewalls. The development is underway and we have observed that more than three** orders of magnitudes **reduction in room-temperature dark current is possible by** passivating with Al_2O_3 **layers**. The results will be reported elsewhere**.**

Table 1. Cross-comparison of device architectures and detection performance between other high-Z energy-sensitive detectors.

	GaSb/AlAsSb	GaSb[1]	GaAs[2]	TlBr[3]	CdTe[4]
Device configuration	SAM	PIN	PIN	Photoresistor	Schottky Diode
Average atomic number	41 (GaSb)	41	31.5	58	50
Surface Area	D = 200 µm (0.1256 mm^2)	D = 200 µm (0.1256 mm^2)	D = 200 µm (0.1256 mm^2)	12.56 mm^2	1024 mm^2
Absorber Thickness (µm)	2	2	3	2000	750
59.5 keV resolution (keV)	1.283	1.789	0.95	1.4	2.33
Temperature (K)	77	140	306	233	265

3. Conclusions

We demonstrated a Sb-based SAM-APD device scheme for X-ray and gamma-ray detection, in which the combination of high-*Z* GaSb absorber and low-*Z*, large bandgap AlAsSb allows a significant enhancement of the probability of stopping high-energy photons while drastically suppressing the device noise. Under ^{241}Am source irradiation, the GaSb/AlAsSb SAM-APDs show clear photopeaks at 59.5 keV with the narrowest FWHM of 1.282±0.082 keV. By decoupling the noise components, we observed that the excess noise (508 eV) was much lower than in the GaSb PIN photodiodes (1245 eV) due to the optimized electric field profile. The FWHM of the 59.5 keV peak can be further improved by eliminating the electronic noise from readout systems. This study provides detailed device characterizations for energy-sensitive GaSb/AlAsSb SAM-APDs and paves the way to achieving efficient detection of high-energy photons for spectroscopy.

Acknowledgements

The authors would like to thank Dr. Benjamin S. Williams for allowing us to use the cryostat chamber. The authors also acknowledge the financial support by the Defense Threat Reduction Agency (DTRA) through award number HDTRA1-14-1-0035 and National Science Foundation of the United States (ECCS-1810507).

Received: ((will be filled in by the editorial staff))
Revised: ((will be filled in by the editorial staff))
Published online: ((will be filled in by the editorial staff))

References

[1] B.-C. Juang, D. L. Prout, B. Liang , A. F. Chatziioannou, D. L. Huffaker, *Appl. Phys. Express* **2016**, *9*, 86401.

[2] A. M. Barnett, *Nucl. Instruments Methods Phys. Res. Sect. A Accel. Spectrometers, Detect. Assoc. Equip*. **2014,** *756*, 39.

[3] M. Shorohov, M. Kouznetsov, I. Lisitskiy, V. Ivanov, V. Gostilo, A. Owens, *IEEE Trans. Nucl. Sci.* **2009,** *56*, 1855.

[4] S. Takeda, M. Katsuragawa, T. Orita, F. Moriyama, Y. Arai, H. Sugawara, S. Oshita, G. Yabu, S. Watanabe, T. Takahashi, L. R. Furenlid, *Nucl. Instruments Methods Phys. Res. Sect. A Accel. Spectrometers, Detect. Assoc. Equip*. **2018,** *912*, 57.

[5] S. W. Cho, Y. B. Kim, S. H. Jung, S. K. Beak, J. S. Kim, M. Lee, H. K. Cho, Y.-H. Kim, *Adv. Opt. Mater.* **2018**, *6*, 1800196.

[6] J. Cai, X. Xu, L. Su, W. Yang, H. Chen, Y. Zhang, X. Fang, *Adv. Opt. Mater.* **2018**, *6*, 1800213.

[7] L. Zheng, W. Zhou, Z. Ning, G. Wang, X. Cheng, W. Hu, W. Zhou, Z. Liu, S. Yang, K. Xu, M. Luo, Y. Yu, *Adv. Opt. Mater.* **2018**, *6*, 1800985.

[8] F. Teng, K. Hu, W. Ouyang, X. Fang, *Adv. Mater.* **2018**, *30*, 1706262.

[9] B. Zhao, F. Wang, H. Chen, L. Zheng, L. Su, D. Zhao, X. Fang, *Adv. Funct. Mater.* **2017**, *27*, 1700264.

[10] W. Ouyang, F. Tang, X. Fang, *Adv. Funct. Mater.* **2018**, *28*, 1707178.

[11] Y. Kang, H.-D. Liu, M. Morse, M. J. Paniccia, M. Zadka, S. Litski, G. Sarid, A. Pauchard,

Y.-H. Kuo, H.-W. Chen, W. S. Zaoui, J. E. Bowers, A. Beling, D. C. McIntosh, X. Zheng, J. C. Campbell, *Nat. Photonics* **2009**, *3*, 59.

[12] J. Michel, J. Liu, L. C. Kimerling, *Nat. Photonics* **2010**, *4*, 527.

[13] Y.-J. Ma, Y.-G. Zhang, Y. Gu, X.-Y. Chen, P. Wang, B.-C. Juang, A. Farrell, B.-L. Liang, D. L. Huffaker, Y.-H. Shi, W.-Y. Ji, B. Du, S.-P. Xi, H.-J. Tang, and J.-X. Fang , *Adv. Opt. Mater.* **2017**, *5*, 1601023.

[14] J. Lauter, D. Protić, A. Förster, H. Lüth, *Nucl. Instruments Methods Phys. Res. Sect. A Accel. Spectrometers, Detect. Assoc. Equip.* **1995**, *356*, 324.

[15] R. B. Gomes, C. H. Tan, X. Meng, J. P. R. David, J. S. Ng, *J. Instrum.* **2014**, *9*, P03014.

[16] T. P. Pearsall, F. Capasso, R. Nahory, M. Pallach, J. Chelikowsky, *Solid-State Electron.* **1978,** *21*, 297.

[17] V. M. Robbins, S. C. Smith, G. E. Stillman, *Appl. Phys. Lett.* **1988,** *52*, 296.

[18] J. P. R. David, J. S. Marsland, J. S. Roberts, *IEEE Electron Device Lett.* **1989**, *10*, 294.

[19] K. A. Anselm, H. Nie, C. Hu, C. Lenox, P. Yuan, G. Kinsey, J. C. Campbell, B. G. Streetman, *IEEE Electron Device Lett.* **1998,** *34*, 482.

[20] A.M. Barnett, J.E. Lees, D.J. Bassforda, J.S. Ngb, *J. Inst.* **2012,** *7*, P06016.

[21] G. Bertuccio, D. Maiocchi, *J. Appl. Phys.* **2002,** *92*, 1248.

[22] B.-C. Juang, D. L. Prout, B. Liang, A. F. Chatziioannou, D. L. Huffaker, *IEEE Device Research Conference* (*DRC)*, Newark, Delaware (June, **2016).**

[23] A. Owens, A. Peacock, *Nucl. Instruments Methods Phys. Res. Sect. A Accel. Spectrometers, Detect. Assoc. Equip*. **2004,** *531*, 18.

[24] S. Butera, G. Lioliou, A. B. Krysa, A. M. Barnett, *Nucl. Instruments Methods Phys. Res. Sect. A Accel. Spectrometers, Detect. Assoc. Equip*. **2018**, *879*, 64.

[25] J. T. South, Z. A. Shellenbarger, M. G. Mauk, J. A. Cox, P. E. Sims, R. A. Mueller, J. D.

Meakin, *AIP Conf. Proc.* **1990,** *460*, 545.

[26] K.-W. Ang, J. W. Ng, G.-Q. Lo, D.-L. Kwong, *Appl. Phys. Lett.* **2009**, *94*, 223515.

[27] B.-C. Juang, B. Liang, D. Ren, D. L. Prout, A. F. Chatziioannou, D. L. Huffaker, *Crystals* **2017**, *7*, 313.

[28] X. Zhou, S. Zhang, J. P. R. David, J. S. Ng, C. H. Tan, *IEEE Photonics Technol. Lett.* **2016**, *28*, 2495.

[29] Y. Zhao, D. Zhang, L. Qin, Q. Tang, R. H. Wu, J. Liu, Y. Zhang, H. Zhang, X. Yuan, W. Liu, *Opt. Express*. **2011,** *19*, 8546

[30] N. Susa, H. Nakagome, H. Ando, H. Kanbe, *IEEE J. Quantum Electron.* **1981,** *17*, 243.

[31] J. Chen, Z. Zhang, M. Zhu, J. Xu, X. Li, *Nanoscale Res. Lett.* **2017,** *12*, 33.

[32] Y. Ma, Y. Zhang, Y. Gu, X. Chen, S. Xi, B. Du, H. Li, *Opt. Express*. **2015**, *23*, 19278

[33] M. S. Ferraro, W. R. Clark, W. S. Rabinovich, R. Mahon, J. L. Murphy, P. G. Goetz, L. M. Thomas, H. R. Burris, C. I. Moore, W. D. Waters, K. Vaccaro, B. D. Krejca, *Appl. Opt.* **2015**, *54*, F182.

[34] W. R. Clark, A. Davis, M. Roland, K. Vaccaro, *IEEE Photonics Technol. Lett.* **2006,** *18*, 19.

[35] G. Bertuccio, P. Rehak, D. Xi, *Nucl. Instruments Methods Phys. Res. Sect. A Accel. Spectrometers, Detect. Assoc. Equip.* **1993,** *326*, 71.

[36] G. Bertuccio, R. Casiraghi, D. Maiocchi, A. Owens, M. Bavdaz, A. Peacock, H. Andersson, S. Nenonen, *IEEE Trans. Nucl. Sci.* **2003,** *50*, 723.